Dilatancy Criteria for Salt Cavern Design: A Comparison Between Stress- and Strain-Based Approaches

P. Labaune[1] · A. Rouabhi[1] · M. Tijani[1] · L. Blanco-Martín[1] · T. You[2]

[1] Centre de Géosciences, MINES ParisTech, PSL Research University, 35 rue St Honoré, 77300 Fontainebleau, France [2] Geostock, 2 Rue des Martinets, 92500 Rueil-Malmaison, France

P. Labaune paule.labaune@mines-paristech.fr

Abstract

This paper presents a new approach for salt cavern design, based on the use of the onset of dilatancy as a design threshold. In the proposed approach, a rheological model that includes dilatancy at the constitutive level is developed, and a strain-based dilatancy criterion is defined. As compared to classical design methods that consist in simulating cavern behavior through creep laws (fitted on long-term tests) and then using a criterion (derived from short-terms tests or experience) to determine the stability of the excavation, the proposed approach is consistent both with short- and long-term conditions. The new strain-based dilatancy criterion is compared to a stress-based dilatancy criterion through numerical simulations of salt caverns under cyclic loading conditions. The dilatancy zones predicted by the strain-based criterion are larger than the ones predicted by the stress-based criteria, which is conservative yet constructive for design purposes.

Keywords: Underground storage, Cavern design, Salt rheology, Dilatancy criteria

$\boldsymbol{I}, \boldsymbol{I}, \boldsymbol{K}$	Orthonormal basis of the stress space
$\boldsymbol{N}$	Deviatoric flow direction
γ_{vp}	Viscoplastic distortion
ζ_{vp}	Viscoplastic volumetric strain
P	Potential function
ϱ	Function defining the shape of the deviatoric section
t	Time
T	Temperature
ρ	Mass density
f	Helmholtz specific free energy
ξ	Discrete set of internal variables

1 Introduction

Underground salt caverns have been used for decades to store hydrocarbons (Bays 1962; Fokker 1995; Thoms and Gehle 2000). In the energy transition context, their design is still a relevant issue. In addition to seasonal or strategic storage of hydrocarbons, other fluids and other forms of energy are stored, such as compressed air or hydrogen, with various

cycling rates (Ozarslan 2012; Djizanne et al. 2014). Caverns are then operated in new ranges of pressures and temperatures, whence the need for accurate design methods.

When designing underground works in rock salt, it has been common practice to address creep behavior and failure separately. Yet these two important aspects of the mechanical behavior of rock salt are strongly linked. In the past years, a commonly applied methodology has consisted in two distinct steps (Wang et al. 2015; Minkley et al. 2016): computation of the stress and strain fields using the strain-hardening behavior of rock salt, and then post-processing of the computed results according to some design criteria.

As part of the first step of cavern design, many creep laws have been developed for rock salt. Their complexity has increased through the years, including new aspects of salt behavior. The first models only defined transient and/or stationary creep strain, such as Norton–Hoff (Bérest et al. 2008), Lemaitre (Tijani et al. 1983), Lubby2 (Heusermann et al. 2003) and Munson–Dawson (Munson and Dawson 1981). Over the years, more phenomena were included, such as dilatancy and healing, for instance in SUVIC (Aubertin et al. 1991), Cristescu (Cristescu 1993), or Günther–Salzer (Günther et al. 2010, 2014). Early models were improved as well: A version of Munson–Dawson (Munson 1993) included inverse creep, and both the MDCF model (DeVries et al. 2002) evolving from Munson–Dawson and Lux–Wolters (Wolters et al. 2012; Wolters 2014) evolving from Lubby2 now include dilatancy, healing and the influence of the Lode angle.

In parallel with creep laws, criteria have been developed to determine the stability (and therefore feasibility) of an excavation. Criteria vary greatly in nature and in their applications. They can be divided into two main categories: the strain-based and the stress-based criteria. Strain-based criteria consist in setting a threshold to a quantity such as the norm of the viscoplastic strain or its rate (Vouille et al. 1993). In turn, stress-based criteria are defined by the stress state. Among these criteria are those based on the dilatancy phenomenon (Van Sambeek et al. 1993; Spiers et al. 1989; Hunsche 1993; Hou 2003; DeVries et al. 2005).

The dilatancy phenomenon is linked to damage, as the inelastic increase in volume is associated with the development of micro-fractures, and consequently a loss of material strength and the development of flow paths (Stormont 1997; Schulze et al. 2001; DeVries et al. 2002). It is exhibited during short-term tests as shown in Fig. 1, which presents results of a triaxial test conducted under a constant confining pressure of 5 MPa and an axial strain rate of $5\times10-6s-15\times10-6s-1$. In the stress space, the stress states corresponding to the onset of dilatancy define, as in the case of yield and failure criteria, a boundary between the contracting and dilating behavior of rock salt. Some well-known stress-based dilatancy criteria are presented in Table 1 and Fig. 2. Stress-based dilatancy criteria are widely

used in feasibility studies, for cavern design (Sobolik and Ehgartner 2011; Moghadam et al. 2013, 2015; Khaledi et al. 2016; Ghasemloonia and Butt 2015; Wang et al. 2016; Yang et al. 2016) as well as for back-calculation of the behavior of underground works (Bauer et al. 1997; Bérest et al. 2008b).

Both strain- and stress-based dilatancy criteria have limitations. Regarding strain-based criteria, their main limitation is their empiricism. The suggested thresholds are often arbitrarily set based on experience and therefore lack strong scientific grounds. As for most stress-based dilatancy criteria, their primary limitation lies in their absence of correlation with creep laws. Indeed, creep tests and in situ strain rates are frequently used to develop and fit creep laws (Heusermann et al. 2003), whereas dilatancy criteria are in general derived from short-term tests (Hunsche 1993). While creep tests are characterized by small strain rates, short-term tests are conducted at much higher rates. The parameter sets derived from both tests are likely unrelated, and therefore the application of such creep laws and dilatancy criteria to cavern design may lead to inconsistencies.

To the best of the authors' knowledge, there does not seem to be any stress-based dilatancy criterion consistent with long-term conditions. In this paper, a methodology is suggested to overcome current limitations and improve cavern design techniques. It is based on the dilatancy phenomenon as its interest in designing structures in rock salt is not questioned. However, only the phenomenological aspects will be considered; no micro-mechanical observation will be made. The proposed methodology consists in taking dilatancy into account at the constitutive level, and using the onset of dilatancy as a design threshold, thus yielding a strain-based dilatancy criterion. This allows addressing both major drawbacks of current criteria: Unlike stress-based dilatancy criteria, it is a single law in agreement with both short- and long-term conditions, and unlike strain-based criteria, the limit is not empirical, but based on an actual rheological phenomenon (i.e., nature of nonelastic volumetric strain rate). This is a purely mechanical study, the thermal and hydraulic aspects are not considered.

This paper first presents a new macroscopic constitutive model for rock salt, based on Lemaitre creep law and extended to account for inelastic volumetric strain. With dilatancy at a constitutive level, the new model allows to define a strain-based dilatancy criterion that can be used for cavern design. The model is able to reproduce short- and long-term tests with a single set of parameters. Then, the new strain-based criterion is compared to a stress-based dilatancy criterion through simulations of laboratory tests, which show that the strain-based criterion is not fixed in the stress space, but evolves over time and depends on the loading history. Finally, the proposed approach is applied to a set of simulations of a simplified cavern under cyclic loading. The results are interpreted in terms of stress- and strain-based dilatancy criteria. Particular attention is given to the effect of the minimum cavern pressure and the cycling rate. All

numerical simulations are performed with the finite element code VIPLEF developed by Mines ParisTech.

2 Constitutive Model

A new constitutive model has been developed in order to study the dilatancy phenomenon. It is based on Lemaitre creep model (Tijani et al. 1983), a commonly used evolution law to describe the viscoplastic behavior of rock salt, and extended to include other mechanisms. We restrict our attention to isotropic models. This framework generally reproduces correctly the phenomenological behavior of rock salt. The stress tensor, denoted by $\boldsymbol{\sigma}$, can be decomposed as[1]:

$$\boldsymbol{\sigma} = \sqrt{2/3}\, q \boldsymbol{J} - \sqrt{3}\, p \boldsymbol{I} \tag{1}$$

where

$$p = -\operatorname{tr}(\boldsymbol{\sigma})/3, \quad q = \sqrt{3/2}||\boldsymbol{\sigma}'|| \qquad \boldsymbol{J} = \boldsymbol{\sigma}'/||\boldsymbol{\sigma}'||, \quad \boldsymbol{I} = \mathbf{1}/\sqrt{3} \tag{2}$$

in which $\boldsymbol{\sigma}'$ is the deviatoric stress tensor, p the mean stress, and q the von Mises equivalent stress. In the Haigh-Westergaard stress space (Chen and Han 1988), the position of the stress point in the deviatoric plane can be identified by the Lode angle $\theta \in [0; \pi/3]$ defined as:

$$\theta = \tfrac{1}{3}\cos^{-1}(\ell), \qquad \ell = \sqrt{6}\operatorname{tr}(\boldsymbol{J}^3) \tag{3}$$

The triaxial extension state of stress corresponds to θ=0 and the triaxial compression state of stress corresponds to θ=π/3.
Either θ∈[0;π/3] or $\ell \in [-1;1]$ can be used, depending on their convenience in the context.

Due to material isotropy, the general form of any scalar isotropic function (plastic potential), which depends on the state of stress $\boldsymbol{\sigma}$, can be expressed in terms of the three particular principal invariants (p,q,θ):

$$P(\boldsymbol{\sigma}) = P(p, q, \theta) \tag{4}$$

For smooth functions, the gradient of $P(\boldsymbol{\sigma})$ with respect to $\boldsymbol{\sigma}$ can be obtained, by involving the chain rule of differential calculus, in the form:

$$\partial_{\boldsymbol{\sigma}} P = -\left(\sqrt{1/3}\,\partial_p P\right)\boldsymbol{I} + \left(\sqrt{3/2}\,\partial_q P\right)\boldsymbol{J} + \left(\sqrt{3/2}\,\partial_\theta P/q\right)\boldsymbol{K} \tag{5}$$

where $\boldsymbol{K}$ is given by:

$$\boldsymbol{K} = \left(\sqrt{2}\boldsymbol{I} + \ell \boldsymbol{J} - \sqrt{6}\boldsymbol{J}^2\right)/\sqrt{1-\ell^2} \tag{6}$$

The three tensors $\boldsymbol{I}$, $\boldsymbol{J}$ and K form an orthonormal basis for the subspace of the symmetric second-order tensors that are coaxial with $\boldsymbol{\sigma}$ when $\boldsymbol{\sigma}$ has three different eigenvalues (the particular cases are q=0: $\boldsymbol{J}$ and $\boldsymbol{K}$ are undefined, and ℓ=±1: $\boldsymbol{K}$ is undefined).

2.1 Viscoplastic Strain Rate Tensor

In the same way as $\boldsymbol{\sigma}$, the viscoplastic strain rate tensor, denoted by $\dot{\boldsymbol{\varepsilon}}_{vp}$ can be decomposed as:

$$\dot{\boldsymbol{\varepsilon}}_{vp} = \sqrt{3/2}\,\dot{\gamma}_{vp}\boldsymbol{N} - \sqrt{1/3}\,\dot{\zeta}_{vp}\boldsymbol{I} \qquad (7)$$

where

$$\dot{\gamma}_{vp} = \sqrt{2/3}\,||\dot{\boldsymbol{\varepsilon}}'_{vp}||, \qquad \dot{\zeta}_{vp} = -\,\mathrm{tr}(\dot{\boldsymbol{\varepsilon}}_{vp}) \qquad (8)$$

The unit tensor $\boldsymbol{N}$ is used to define the deviatoric flow direction which in this work is assumed to be defined independently of the spherical part of $\dot{\boldsymbol{\varepsilon}}_{vp}$. It is defined in terms of the gradient of a potential function $P(\boldsymbol{\sigma})$ of the form:

$$P(\boldsymbol{\sigma}) = P(q,\theta) = q/\varrho(\theta) \qquad (9)$$

where $\varrho(\theta)$ is a scalar function that describes the Lode angle dependency. More explicitly, by using Eq. (5), the tensor N can be written as[2]:

$$\boldsymbol{N} = \partial_{\sigma}P/||\partial_{\sigma}P|| = \left(\boldsymbol{J} - (\varrho'/\varrho)\boldsymbol{K}\right)/\sqrt{1+(\varrho'/\varrho)^2} \qquad (10)$$

It is noteworthy that the flow rule (Eq. 7) allows great freedom in the depiction of phenomena, especially those involving material contractancy and dilatancy. The only restriction comes from thermodynamics, which states that the intrinsic dissipation must be positive:

$$\boldsymbol{\sigma} : \dot{\boldsymbol{\varepsilon}}_{vp} - \rho\partial_{\xi}f\dot{\xi} \geq 0 \qquad (11)$$

where ρ is the mass density and f is the Helmholtz specific free energy, assumed here to be function of $\boldsymbol{\sigma}$, of temperature T and of a discrete set of internal variables ξ that characterize the material history. This thermodynamic restriction can give rise to a wide range of rheological behavior since we can choose $f(\boldsymbol{\sigma},T,\xi)$ in a way that always satisfies this condition. Notice that the term $\boldsymbol{\sigma} : \dot{\boldsymbol{\varepsilon}}_{vp}$ can be expressed as:

$$\boldsymbol{\sigma} : \dot{\boldsymbol{\varepsilon}}_{vp} = p\dot{\zeta}_{vp} + q\dot{\gamma}_{vp}\cos(\theta - \theta_{\varepsilon}) \qquad (12)$$

where θ_ε is the Lode angle of $\dot{\boldsymbol{\varepsilon}}_{vp}$, and thus under triaxial conditions ($\theta=\theta_\varepsilon$), Eq. (12) is reduced to the well-known dissipation equality generally used in soil behavior modeling.

To fully define the evolution of the viscoplastic strain rate, the function $\varrho(\theta)$ still needs to be defined, as well as the variables γ_{vp} and ζ_{vp}. This will be done, respectively, in Sects. 2.2 and 2.3.

2.2 Lode Angle Dependency

The function ϱ defines the shape of the deviatoric section of the potential $P(q,\theta)$. Bigoni and Piccolroaz (2004) suggest an expression for ϱ, using two parameters $\chi_1 \in [0,1]$ and $\chi_2 \in [0,2]$:

$$\varrho(\theta) = \varrho(\ell(\theta)) = \frac{\cos\left(\frac{\pi}{6}\chi_2 - \frac{1}{3}\arccos(-\chi_1 \ell)\right)}{\cos\left(\frac{\pi}{6}\chi_2 - \frac{1}{3}\arccos(\chi_1 \ell)\right)} \qquad (13)$$

The function $\varrho(\theta)$ is defined for all $\theta \in [0;\pi/3]$ and extended by symmetry to $[0;2\pi]$. The case $\ell=-1$ being the triaxial compression state of stress, the function ϱ is normalized to equal 1 in compression for all values of χ_1 and χ_2. Figure 3 shows the shape of the deviatoric section for different values of χ_1 and χ_2. From Eq. (13), when $\chi_1=0$, $\varrho(\theta)=1$ for all θ regardless of the value of χ_2 and the deviatoric section is a circle. This means that for all θ, $\boldsymbol{N}=\boldsymbol{J}$, so the state of stress (compression, extension, etc.) has no influence on the direction of strain. Another particular case is when χ_2 tends to 0 and χ_1 tends to 1, the deviatoric section tends to a triangle. However, this case should be avoided since it can lead to numerical difficulties associated with gradient calculation. An asymmetry has been thereby introduced between compression ($\theta=\pi/3$) and extension ($\theta=0$).

2.3 Internal Variables

We assume that the material past history is represented only by the viscoplastic distortion, γ_{vp}. The local thermodynamic state is thus defined by $(\boldsymbol{\sigma},\boldsymbol{T},\gamma_{vp})$. We also assume that the ratio $d\zeta_{vp}/d\gamma_{vp}$ depends only on the thermodynamic state. These hypotheses allow us to write γ_{vp} and ζ_{vp} as:

$$\dot{\gamma}_{vp} = \dot{\gamma}_{vp}(\boldsymbol{\sigma}, T, \gamma_{vp}) \qquad \dot{\zeta}_{vp} = \varphi(\boldsymbol{\sigma}, T, \gamma_{vp})\dot{\gamma}_{vp} \qquad (14)$$

with $\varphi(\boldsymbol{\sigma},\boldsymbol{T},\gamma_{vp})$ a function to be defined. Note that this definition of ζ_{vp} implies that the viscoplastic volumetric strain only varies if there is an evolution of distortion.

The evolution of γ_{vp} is a generalization of Lemaitre model, enriched with an influence of the mean pressure p and the Lode angle θ:

$$\frac{\mathrm{d}\gamma_{vp}^{1/a}}{\mathrm{d}t} = \left(\psi(\boldsymbol{\sigma}, T, \gamma_{vp})\right)^{1/a}$$
$$\psi(\boldsymbol{\sigma}, T, \gamma_{vp}) = \mathrm{e}^{A\left(\frac{1}{T_r}-\frac{1}{T}\right)}\left\langle \frac{q/\varrho(\theta) - B\gamma_{vp}^{b}p}{K} \right\rangle^{k} \qquad (15)$$

where $\langle\cdot\rangle$ are the Macaulay brackets, i.e., $\langle x\rangle=(x+|x|)/2$.
Parameters A, T_r, a, b, B, k and K are positive material constants. The mean pressure effect is taken into account through the term $B\gamma_{vp}^{b}\dot{p}$, which allows reproducing correctly the effect of the confining pressure during short-term tests, as well as the effect of the deviatoric stress during multistage creep tests. Note also that the influence of the state of stress is taken into account by adding function $\varrho(\theta)$ [defined in Eq. (13)]. This function adds asymmetry in the hardening: All else being equal, viscoplastic strain is greater in extension than it is in compression.

Regarding ζ_{vp}, its evolution is defined through the function φ, which is also defined based on experimental results:

$$\varphi(\boldsymbol{\sigma}, T, \gamma_{vp}) = \min\left(v\frac{\left(\langle p\rangle/N\right)^{n} - \gamma_{vp}}{\left(\langle p\rangle/M\right)^{m} + \gamma_{vp}}, V \right) \qquad (16)$$

where parameters v, V, n, N, m and M are positive material constants. The parameters N and n define a dilatancy threshold: the viscoplastic volumetric strain rate changes sign when $\gamma_{vp}=(\langle p\rangle/N)^{n}$, moving from a contracting to a dilating behavior. Remaining parameters v, M and m allow to better adjust the shape and magnitude of the volumetric strain. Parameter V is a threshold to prevent excessive volumetric strains under low mean stresses.

Overall, the proposed model defined through Eqs. (1–16) includes dilatancy from a constitutive point of view and the influence of the Lode angle. It can be reduced to the classic version of Lemaitre model by setting $\chi_1=0$, $B=0$, $v=0$.

2.4 Parameters Fitting

In order to show the capabilities of the new model to fit simultaneously short- and long-term tests, which is a major challenge for creep constitutive models in general, we present a fitting example of tests performed in our department on Landes salt (South West France). Since the stress state was compressive during all the tests, the parameters related to the deviatoric section χ_1 and χ_2 could not be fitted. They were arbitrarily set to $\chi_1=0.7$ and $\chi_2=0$. Likewise the temperature being constant, parameter A could not be fitted and was set to 0. The elastic parameters E and ν were fitted using the unloading/reloading cycles of the

short-term triaxial tests. The remaining parameters were fitted in two independent steps: the fitting of γ_{vp} for the parameters related to distortion, and the fitting of ζ_{vp} for the parameters related to dilatancy. It can be noted that, since the expression of ζ_{vp} includes γ_{vp}, it can be fitted in two different ways: using the previously fitted values for γ_{vp}, or the experimental values. We decided to use the experimental values because it ensures the independence of the two fittings. All the model parameters are determined using an error minimization procedure based on the least square method.

As an illustration, a series of fittings is presented here: experimental data and fitted curves are shown in Fig. 4 and the parameter set is given in Table 2. Four tests were fitted simultaneously: three short-term triaxial tests and one creep test. The short-term tests were carried out at the same axial strain rate of 5×10^{-6} s^{-1} and constant confining pressure of, respectively, 5, 10 and 15 MPa. The creep test was performed at constant confining pressure (5 MPa) with three stages of deviatoric stress (5, 10 and 15 MPa).

In addition to the constitutive model adjustments, a stress-based dilatancy criterion is fitted on the same experimental data. Given the available data, a linear criterion is chosen. Figure 5shows experimental points, corresponding to the onset of dilatancy for twelve short-term tests, as well as the fitted dilatancy criterion.

2.5 Simulations of Uniformly Strained Laboratory Tests

The proposed model allows to define a strain-based dilatancy criterion. Indeed, $\dot{\zeta}_{vp}=0$ corresponds to the onset of dilatancy and $\dot{\zeta}_{vp}<0$ corresponds to dilating conditions. This new criterion exhibits naturally the dependence on the loading rate unlike stress-based dilatancy criteria which are rate independent. In order to show the difference between the two criteria, constant mean stress tests are simulated and the dilatancy limit is studied. During such tests the measured total and viscoplastic volumetric strains are equal, and therefore the determination of the onset of dilatancy is straightforward (DeVries et al. 2005). Practically, to keep the mean stress constant, the confining pressure is lowered (respectively, increased) as the axial pressure is increased (respectively, lowered). Tests are terminated when one of the pressures reaches zero. All simulations are carried out under isothermal conditions using the parameter set defined in the previous section (Table 2).

A total of thirty-two constant mean stress tests are simulated, exploring four different levels of mean stress, two stress states (compression and extension), and four loading rates. The mean stress values, 10 to 25 MPa, were chosen as high as what is commonly seen in laboratory testing, and as low as possible. Indeed, for mean stress values lower than 10 MPa, one of the stresses would reach zero before reaching the onset of dilatancy. The four loading rate values match loading rates typically found either in laboratory testing (high rates) and in salt caverns (low rates).

For each test the onset of dilatancy was identified and plotted in the $p-q$ plane, shown in Fig. 6, where we added the stress-based criterion derived from the experimental data (Fig. 5). As expected, besides the fact that the dilatancy limit increases with the mean pressure and is lower in extension than in compression, it is strongly affected by the loading rate: the slower the test, the lower the dilatancy limit. This needs to catch our attention, as the majority of experimental tests at laboratory-scale is carried out in a compression state of stress, with higher rates than classic in situ loading rates. As Fig. 6 shows, using an experimentally defined stress-based dilatancy criterion based on high-speed constant mean stress tests could lead to a severe underestimation of dilatancy.

3 Application to Cavern Design

Simulations of a salt cavern for gas storage are carried out to show the differences in dilatancy zones as predicted by criteria based on stress or based on strain. We call dilatancy zones all the points such that the dilatancy criterion is exceeded. They represent zones where the mechanical integrity is compromised, and in which micro-fractures could develop with potential detrimental impacts on flow properties. For the stress-based dilatancy criterion, we use the one fitted on the experimental results as explained in the previous Section. The strain-based criterion is the one derived from the new model.

This section focuses on two major issues in cavern operation: the value of the minimum gas pressure, and the cycling rate. Concerning the minimum gas pressure, choosing a value around 20% of the geostatic pressure is fairly common (Serbin et al. 2015). However, lower values allow to be more economically profitable and more conservative from a cavern design perspective, even in the case of catastrophic scenarios such as blowouts during which the cavern pressure can drop quickly and remain as low as the atmospheric pressure for large amounts of time (Bérest et al. 2013). As for the cycling rate, besides the classical seasonal storage, in the energy transition context salt caverns are expected to operate with higher cycling rates and deliverability.

3.1 Modeling Setup

The simulated cavern is based on data from existing gas storage caverns [see, for instance, (Thoms and Gehle 2000; Bérest et al. 2012)]. It does not represent one existing cavern in particular but its characteristics were chosen using in situ data in terms of depth, shape, volume, and operating conditions.

The geometry was simplified and made axisymmetric; the initial volume is about 200,000 m^3 and the average depth 1500 m. The simulated domain includes rock salt from the surface to a depth of 3000 m and a lateral extension of 3000 m. A close-up of the geometry and mesh around the cavern are presented in Fig. 7. Far from the cavern the stress state is

isotropic and equal to the geostatic pressure. The pressure inside the cavern is controlled to simulate the successive phases of cavern exploitation: leaching, dewatering, then cycles of gas withdrawal/injection as it can be seen in Fig. 8. The leaching phase is simulated by slowly lowering the cavern pressure from the geostatic pressure to the brine pressure over a period of 500 days. The dewatering phase is simulated by increasing the cavern pressure to the dewatering pressure over a period of 50 days. Then the pressure is brought to the maximum gas pressure to simulate the first fill. Finally, cycles of gas withdrawal/filling are simulated, alternatively decreasing and increasing the cavern pressure between the minimum (P_{min}) and the maximum (P_{max}) gas pressure. The duration of each phase may vary, as well as the values of P_{min} and P_{max}. For the base case, we consider cycles of 400 days: the cavern pressure is held constant at P_{max} for 180 days, lowered to P_{min} over 20 days, held constant at P_{min} for 180 days, and increased to P_{max} over 20 days. The value of P_{max} is chosen to 80% of the geostatic pressure, and P_{min} is set to 0, which is extreme but this value was chosen to emphasize all strains in the surroundings of the cavern. The simulation is terminated after a total of 10,000 days. The material parameters are given in Table 2. All simulations are run under isothermal conditions.

3.2 Influence of Dilatancy on Cavern Closure

Before studying dilatancy zones around the cavern and comparing dilatancy criteria, we shall first show that the addition of a volumetric component to the viscoplastic strain rate tensor $\dot{\boldsymbol{\varepsilon}}_{vp}$ does not excessively change the results.

Two simulations of the same cavern with the same loading history are carried out. They are identical except for the volumetric component of $\dot{\boldsymbol{\varepsilon}}_{vp}$: the first one uses the parameter set given in Table 2, whereas in the second one parameter v is set to 0. Comparing results of these two simulations allows to evaluate the influence of the addition of the spherical part $\zeta \mathbf{I}_{vp}$ to the model [see Eq. 16].

Figure 9 shows the cavern volume variation over time for both simulations ($v \neq 0$ and $v = 0$). The volume of the cavern is overall decreasing and the closing rate decreases over time. When the pressure in the cavern quickly increases or decreases, so does the cavern volume due to elastic strain. When the pressure is held at maximum gas pressure, the volume is almost steady, and when pressure is held at minimum gas pressure, the volume decreases by creep. The difference in volume loss between the two simulations is very limited: After 10,000 days the cavern loss is around 18%, and the difference between the two simulations does not exceed 0.3%. Therefore, the addition of a volumetric component to the viscoplastic strain rate does not have a substantial impact on the global behavior of the cavern. Indeed, the majority of the cavern closure is due to salt flowing from

the surroundings (because of the deviatoric stresses), and not to the dilatancy of the salt in the vicinity of the cavern.

3.3 Comparison Between the Stress- and Strain-Based Criteria

In what follows we focus on the simulation having $v \neq 0$ and study the dilatancy zones according to the stress- and strain-based dilatancy criteria. For the stress-based criterion, the dilatancy zone is formed by all the points verifying $q \geq 1.3p + 2.5$ [see Fig. 5]; for the strain-based criterion, the dilatancy zone corresponds to all points such that $\dot{\zeta}_{vp} \leq 0$ [see Eqs. (14) and (16)].

Figure 10 shows the evolution of the width of the dilatancy zone normalized with respect to the radius of the cavern, according to the stress-based and the strain-based dilatancy criteria. Both criteria agree that there is no dilatancy in the leaching, dewatering, and first filling phases. According to the strain-based criterion, the width of the dilatancy zone quickly grows at the beginning of the cyclic loading and stabilizes slightly below a distance of two times the cavern radius. On the other hand, the evolution of the width of the dilatancy zone according to the stress-based criterion is completely different. Dilatancy zones appear and disappear throughout each cycle: they are nonexistent when the cavern pressure is $P_{\max}$, and their width is maximum when the cavern pressure is $P_{\min}$. From one cycle to another there is very little change in the extent of the dilatancy zone, its maximum width remains stable around 30% of the cavern radius.

Figure 11 shows the same result in space: The dilatancy limit is plotted around the cavern for both criteria at the end of the gas withdrawal phase for the first two cycles and then every third cycle until the end of the simulation. For the stress-based criterion, the dilatancy limit is the isovalue such that $q = 1.3p + 2.5$; for the strain-based criterion, it is the isovalue such that $\dot{\zeta}_{vp} = 0$. In agreement with Fig. 10, the stress-based dilatancy limit remains virtually constant. According to the strain-based criterion, however, the dilatancy zone grows over time, quickly at the beginning and slowly as time goes on. Dilatancy zones may seem excessively large, but it is important to keep in mind that the base case scenario considers a value of $P_{\min} = 0$, which is purposely excessive.

We note that instead of studying the limit $\dot{\zeta}_{vp} = 0$, which considers the onset of dilatancy, we could have studied the limit $\zeta = 0$, which considers the moment when rock salt is back to its initial volume and starts dilating. Conceptually, the corresponding point can be seen in Fig. 1. Such damage zones are smaller than dilatancy zones.

3.4 Effect of Minimum Gas Pressure

Another series of simulations is carried out in order to study the effect of the minimum gas pressure on dilatancy zones and how it is taken into account by stress-based and strain-based criteria. The geometry, loading history, and rheological parameters are the same as described in Sect. 3.3, only the

value of the minimum gas pressure P_{min} varies. The values investigated are P_{min} =0, 3 and 6 MPa, which represent 0, 10 and 20% of the geostatic pressure, respectively.

Figure 12 shows the evolution of the stress state at the cavern wall in a $p-q$ diagram for the three values of P_{min}. For P_{min} =6 MPa the stress-based dilatancy criterion is never reached, for P_{min} =3 MPa it is just barely reached, and for P_{min} =0 MPa it is clearly exceeded for a significant portion of each cycle.

Figure 13 shows the dilatancy zones around the cavern in time (left) and in space (right), for both dilatancy criteria. For the stress-based criterion, the results are consistent with Fig. 12: for a high value of P_{min} the dilatancy boundary is never reached, for an intermediate value it is barely reached, and when P_{min} =0 it is exceeded at each cycle for about a distance of 0.3 times the cavern radius. The strain-based criterion predicts much larger dilatancy zones. Yet their evolution is consistent with the stress-based criterion, dilatancy zones grow as P_{min} lowers. These observations are in agreement with the phenomenon illustrated in Fig. 6: reducing P_{min} leads to lowering the mean pressure p and increasing the deviatoric stress q, which is favorable to initiate dilatancy.

It must be noted that, in the case of a low minimum pressure, although the dilatancy zone is large, its width stabilizes over time, which is encouraging from a cavern design perspective.

3.5 Effect of Cycling Rate

Additional simulations are carried out to study the effect of the cycling rate. These simulations are similar to the previous ones, the minimum pressure P_{min} is set to 0 and only the loading history varies. Here, the base case scenario (400-day cycles) is compared with a simulation having 10-day cycles, keeping the same time ratio between each cycle phase: 4.5 days at P_{max}, 0.5 day withdrawal, 4.5 days at P_{min}, 0.5 days refill.

Figure 14 shows the evolution of the stress state at the cavern wall in the $p-q$ diagram for both 400-day and 10-day cycles. The stress state around the cavern is similar in both cases.

Figure 15 shows the evolution of the width of the dilatancy zone for both cycling rates and both dilatancy criteria. For the stress-based criterion, no significant difference can be seen between short and long cycles, as in Fig. 14. However, for the strain-based criterion, the cycling rate does influence the size of the dilatancy zone: For long cycles it stabilizes slightly below twice the cavern radius, while for short cycles it ends around 1.6 times the cavern radius. From a purely mechanical point of view, high cycling rates actually lead to smaller dilatancy zones. A thermomechanical study should bring more insight to this issue.

Finally, Fig. 16 shows the dilatancy limit around the cavern at the end of the first gas withdrawal phase, for both long and short cycles, and both dilatancy criteria. For short cycles, both criteria provide fairly similar results, but for long cycles the strain-based criteria predicts a dilatancy zone approximately twice as wide. These observations are in agreement with the rate-dependency illustrated in Fig. 6, since the stress criterion is based on experimental tests conducted at high strain rates compared to seasonal cycling rates. It is consistent that both criteria match when the strain rate is high, but diverge in the case of a low cycling rate.

Open image in new window

4 Conclusion and Perspectives

This paper presents a new approach for salt cavern design, based on the use of the onset of dilatancy as a design threshold. A new constitutive model has been developed based on Lemaitre creep law and including dilatancy, thereby allowing to define a strain-based dilatancy criterion (onset of dilatancy when $\mathrm{tr}(\dot{\boldsymbol{\varepsilon}}_{vp}) = 0$). The new model is able to reproduce short- and long-term tests with a single set of parameters; therefore, unlike existing stress-based dilatancy criteria, the new criterion is consistent with both short- and long-term conditions. Moreover, unlike other strain-based criteria the threshold is not empirical, but based on a tangible rheological phenomenon of dilatancy.

A comparison between the new strain-based dilatancy criterion and a common stress-based dilatancy criterion highlights two major differences. First, the strain-based criterion depends on the loading history and evolves over time, whereas any stress-based criterion remains fixed in the stress space. Second, the dilatancy zones predicted by the strain-based criterion are larger than the ones predicted by the stress-based criterion, which is conservative from a cavern design perspective.

Several simulations of a salt cavern under cyclic loading were performed, and the results were analyzed in terms of the two criteria. Two issues were studied in particular: the influence of the minimum pressure P_{min}, and of the cycling rate. Qualitatively the same trends can be observed: The magnitude of dilatancy zones increases when P_{min} decreases. Yet the magnitude of the dilatancy zones predicted by the two criteria does not match. Concerning the cycling rate, the two criteria are in agreement in early stages if the strain rates are high enough (and then diverge over time). However, in case of lower cycling rates, the strain-based criterion predicts much larger dilatancy zones than the stress-based criterion from the beginning. All these facts are important as the choice of P_{min} is a major issue in cavern design, and not considering the loading rate in the constitutive model can lead to an underestimation of dilatancy. Indeed, most laboratory tests are carried out at much higher strain rates than the ones observed *in situ*.

Perspectives of this research include thermomechanical analysis (instead of purely mechanical) as temperature has an important influence on salt behavior. The authors also seek to add improvements to their rheological model to account for more thermomechanical phenomena such as inverse creep or healing.

Footnotes

[1] For any tensor $\boldsymbol{a}$, its deviatoric part is designated by a prime: $\boldsymbol{a}' = \boldsymbol{a} - \frac{1}{3}\mathrm{tr}(\boldsymbol{a})\mathbf{1}$, where $\mathbf{1}$ is the identity tensor and $\mathrm{tr}(-)$ denotes the trace operator, and its norm is designated by $||\boldsymbol{a}|| = \sqrt{\boldsymbol{a} : \boldsymbol{a}}$.

[2] The notation $f'(x)$ indicates the derivative of f with respect to x.

References

Aubertin M, Gill DE, Ladanyi B (1991) A unified viscoplastic model for the inelastic flow of alkali halides. Mech Mater 11(1):63–82

Bauer SJ, Ehgartner BL, Neal JT (1997) Geotechnical studies associated with decommisioning the strategic petroleum reserve facility at Weeks Island, Louisiana: a case history. Int J Rock Mech Min Sci 34(3–4):25-e1

Bays C (1962) Use of salt solution cavities for underground storage. In: Proceedings of the first world salt symposium, Cleveland, OH. pp 564–578

Bérest P, Brouard B, Feuga B, Karimi-Jafari M (2008a) The 1873 collapse of the Saint-Maximilien panel at the Varangeville salt mine. Int J Rock Mech Min Sci 45(7):1025–1043

Bérest P, Karimi-Jafari M, Brouard B (2008b) Comportement mécanique à très long terme des mines et cavernes dans le sel gemme : loi de Norton-Hoff ou loi de Lemaitre. Revue Française de Géotechnique 1(124):45

Bérest P, Djakeun-Djizanne H, Brouard B, Hévin G (2012) Rapid depresurizations: Can they lead to irreversible damage? In: SMRI spring conference, 23–24 April 2012

Bérest P, Djakeun-Djizanne H, Brouard B, Frangi A (2013) A simplified solution for gas flow during a blow-out in an H2 or air storage cavern. In: SMRI spring conference, 22–23 April 2013. pp 125–144

Bigoni D, Piccolroaz A (2004) Yield criteria for quasibrittle and frictional materials. Int J Solid Struct 41(11):2855–2878

Chen WF, Han DJ (1988) Plasticity for structural engineers. Springer, New York

Cristescu N (1993) A general constitutive equation for transient and stationary creep of rock salt. Int J Rock Mechan Min Sci Geomechan Abstr 30(2):125–140

DeVries KL, Mellegard KD, Callahan GD (2002) Salt damage criterion proof-of-concept research. Technical Report DE-FC26-00NT41026, RESPEC, Rapid City, South Dakota

DeVries KL, Mellegard KD, Callahan GD, Goodman WM (2005) Cavern roof stability for natural gas storage in bedded salt. Technical Report DE-FG26-02NT41651, RESPEC, Rapid City, South Dakota

Djizanne H, Bérest P, Brouard B (2014) The mechanical stability of a salt cavern used for compressed air energy storage (CAES). In: SMRI spring 2014 technical conference, San Antonio, Texas, USA

Fokker PA (1995) The behaviour of salt and salt caverns. Ph.D. Dissertation, Delft University of Technology

Ghasemloonia A, Butt S (2015) Feasibility study of underground salt caverns in Western Newfoundland: experimental and finite element investigation of creep-induced damage. J Min Environ 6(2):205–224

Günther R, Salzer K, Popp T (2010) Advanced strain-hardening approach constitutive model for rock salt describing transient, stationary, and accelerated creep and dilatancy. In: 44th US rock mechanics symposium and 5th US-Canada rock mechanics symposium. American Rock Mechanics Association

Günther R, Salzer K, Popp T, Lüdeling C (2014) Steady state-creep of rock salt—improved approaches for lab determination and modeling to describe transient, stationary and accelerated creep, dilatancy and healing. In: 48th US rock mechanics/geomechanics symposium. American Rock Mechanics Association

Heusermann S, Rolfs O, Schmidt U (2003) Nonlinear finite-element analysis of solution mined storage caverns in rock salt using the Lubby2 constitutive model. Comput Struct 81(811):629–638

Hou Z (2003) Mechanical and hydraulic behavior of rock salt in the excavation disturbed zone around underground facilities. Int J Rock Mech Min Sci 40(5):725–738

Hunsche UE (1993) Failure behaviour of rock salt around underground cavities. In: Proceedings of the 7th symposium on salt, vol 1. pp 59–65

Khaledi K, Mahmoudi E, Datcheva M, Schanz T (2016) Stability and serviceability of underground energy storage caverns in rock salt subjected to mechanical cyclic loading. Int J Rock Mech Min Sci 86:115–131

Minkley W, Mühlbauer J, Lüdeling C (2016) Dimensioning principles in potash and salt: stability and integrity. Rock Mech Rock Eng 49(11):4537–4555

Moghadam SN, Mirzabozorg H, Noorzad A (2013) Modeling time-dependent behavior of gas caverns in rock salt considering creep, dilatancy and failure. Tunn Undergr Space Technol 33:171–185

Moghadam SN, Nazokkar K, Chalaturnyk RJ, Mirzabozorg H (2015) Parametric assessment of salt cavern performance using a creep model describing dilatancy and failure. Int J Rock Mech Min Sci 79:250–267

Munson DE (1993) Extension of the M-D model for treating stress drops in salt. In: Third conference on the mechanical behavior of salt. Ecole Polytechnique, Palaiseau, France, pp 31–44

Munson DE, Dawson PR (1981) Salt constitutive modeling using mechanism maps. In: First conference on the mechanical behavior of salt. pp 717–737, Pennsylvania State University

Ozarslan A (2012) Large-scale hydrogen energy storage in salt caverns. Int J Hydrog Energy 37(19):14265–14277

Schulze O, Popp T, Kern H (2001) Development of damage and permeability in deforming rock salt. Eng Geol 61(2):163–180

Serbin K, Ślizowski J, Urbańczyk K, Nagy S (2015) The influence of thermodynamic effects on gas storage cavern convergence. Int J Rock Mech Min Sci 79:166–171

Sobolik SR, Ehgartner BL (2011) In: Technical conference. Galveston, Texas, USA

Spiers C, Peach C, Brzesowsky R (1989) In: Long-term rheological and transport properties of dry and wet salt rocks: final report. Office for Official Publications of the European Communities

Stormont J (1997) In situ gas permeability measurements to delineate damage in rock salt. Int J Rock Mech Min Sci 34(7):1055–1064

Thoms R, Gehle R (2000) A brief history of salt cavern use. In: Geertman R (ed) Proceedings of the 8th world salt symposium, The Hague. pp 207–214

Tijani M, Vouille G, Hugout B (1983) Le sel gemme en tant que liquide visqueux. In: Congrès International de Mécanique des Roches, Melbourne. pp 241–246

Van Sambeek LL, Ratigan JL, Hansen FD (1993) Dilatancy of rock salt in laboratory tests. Int J Rock Mech Min Sci Geomech Abstr 30(7):735–738

Vouille G, Bergues J, Durup G, You T (1993) Study of the stability of caverns in rock salt created by solution mining-proposal for a new design criterion. In: ISRM international symposium-EUROCK 93. International Society for Rock Mechanics

Wang L, Bérest P, Brouard B (2015) Mechanical behavior of salt caverns: closed-form solutions vs numerical computations. Rock Mech Rock Eng 48(6):2369–2382

Wang T, Yang C, Ma H, Li Y, Shi X, Li J, Daemen J (2016) Safety evaluation of salt cavern gas storage close to an old cavern. Int J Rock Mech Min Sci 83:95–106

Wolters R (2014) Thermisch-hydraulisch-mechanisch gekoppelte Analysen zum Tragverhalten von Kavernen im Salinargebirge vor dem Hintergrund der Energieträgerspeicherung und der Abfallentsorgung. Ph.D. Dissertation, Technischen Universität Clausthal

Wolters R, Lux K, Düsterloh U (2012) Evaluation of rock salt barriers with respect to tightness: influence of thermomechanical damage, fluid infiltration and sealing/healing. In: Proceedings of the seventh international conference on the mechanical behavior of salt, Paris, 16–19 April 2012, pp 425–434

Yang C, Wang T, Ma H, Li Y, Shi X, Daemen J (2016) Feasibility analysis of using horizontal caverns for underground gas storage: a case study of Yunying salt district. J Nat Gas Sci Eng 36:252–266

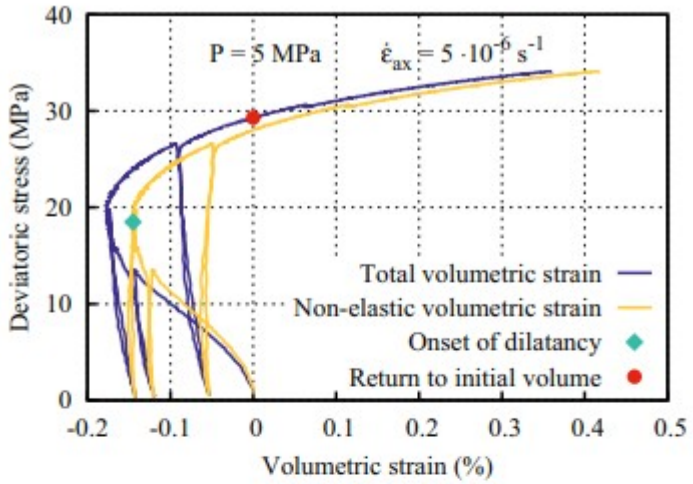

Fig. 1 Experimental data showing dilatancy during a short-term triaxial test on Landes salt (test conducted at Mines ParisTech). The onset of dilatancy occurs when the sign of the inelastic volumetric strain rate changes. Compressive strains and stresses are negative

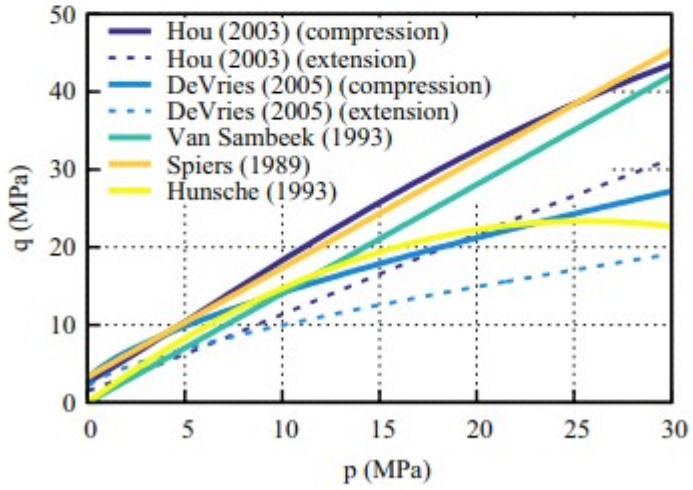

Fig. 2 Examples of dilatancy criteria plotted in the $p - q$ plane

Table 1 Examples of dilatancy criteria, where p, q and θ are three invariants of the stress tensor defined in Sect. 2 [see Eqs. (2) and (3)]

$q = ap + b$	
$a = 1.4, \quad b = 0\,\text{MPa}$	Van Sambeek et al. (1993) (WIPP)
$a = 1.4, \quad b = 3.3\,\text{MPa}$	Spiers et al. (1989) (Asse)
$q = ap^2 + bp$	
$a = -0.0356\,\text{MPa}^{-1}, \quad b = 1.82$	Hunsche (1993) (Asse)
$q = \eta_D(\sigma_3)\,\beta^{TC}(\sigma_3)\,k_\beta(\sigma_3, \theta), \qquad p = \sigma_3 + (2/3)q\cos(\theta)$	
$\eta_D = 1 - a_4 \exp(a_5\sigma_3), \quad \beta^{TC} = a_6 - a_7 \exp(a_8\sigma_3)$	
$k_\beta = (\cos(\pi/3 - \theta) + a_9 \sin(\pi/3 - \theta))^{-\exp(a_{10}\sigma_3)}$	
$a_4 = 0.8, \quad a_5 = 0.055\,\text{MPa}^{-1}, \quad a_6 = 67\,\text{MPa}, \quad a_7 = 41\,\text{MPa}$	Hou (2003) (Asse)
$a_8 = 0.25\,\text{MPa}^{-1}, \quad a_9 = 1, \quad a_{10} = 0.25\,\text{MPa}^{-1}$	
$q = \frac{a(\lvert p\rvert/\sigma_0)^n + b}{\cos(\pi/3-\theta) + c\sin(\pi/3-\theta)}$	
$a = 2.316\,\text{MPa}, \quad b = 2.728\,\text{MPa}, \quad c = 1.066$	DeVries et al. (2005) (Cayuta)
$n = 0.693, \quad \sigma_0 = 1\,\text{MPa}$	

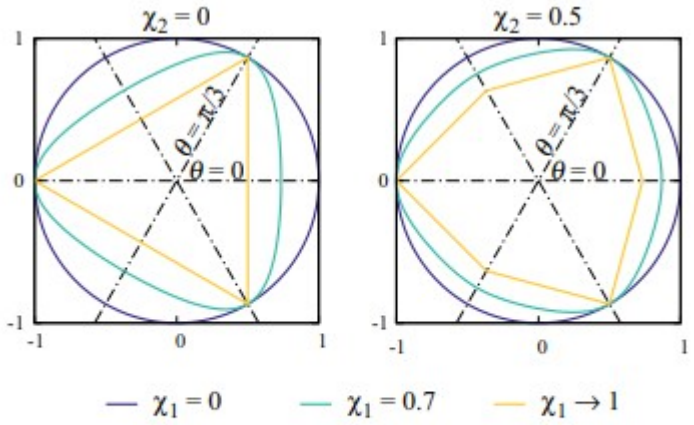

Fig. 3 Deviatoric cross section of the potential surface $P(\boldsymbol{\sigma}) = q/\varrho(\theta)$ for $\chi_2 = 0, 0.5$ and $\chi_1 = 0, 0.7, 1$

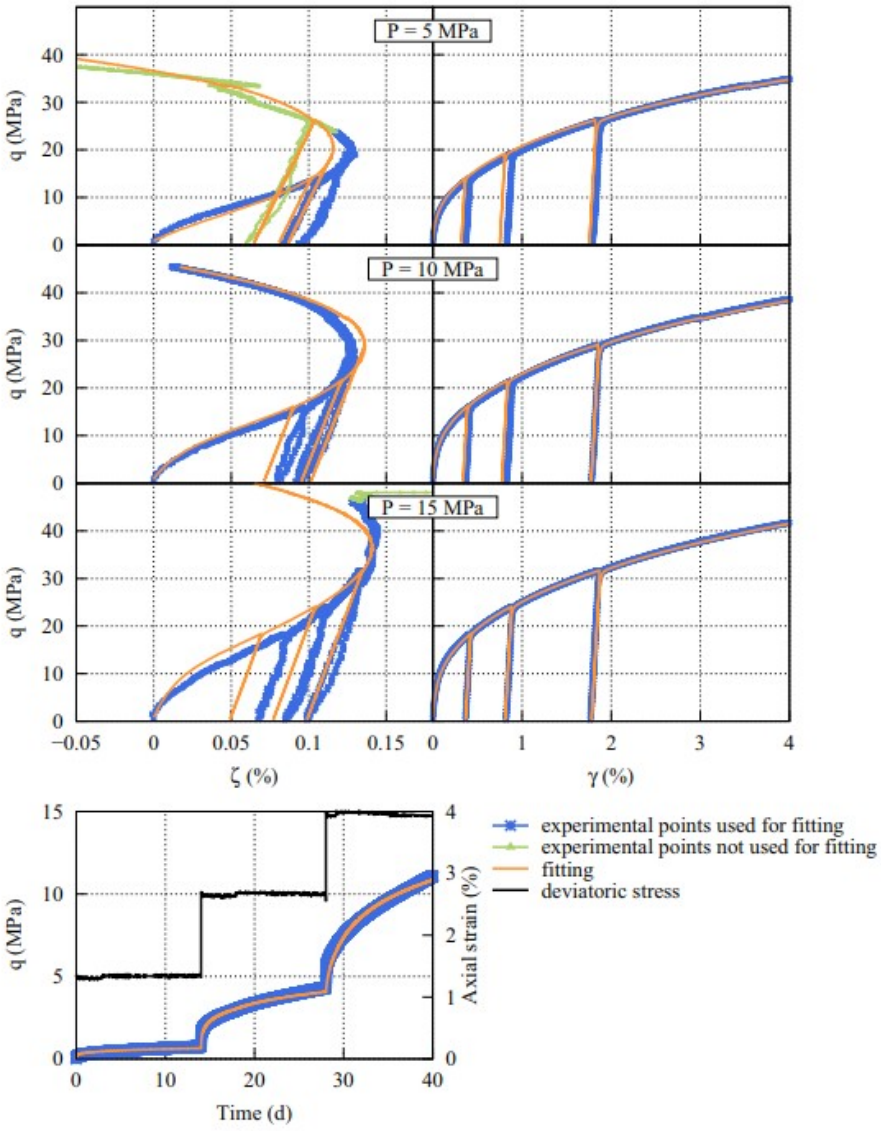

Fig. 4 Fitting of three short-term triaxial tests (top) and one multistage creep test (bottom) with a single parameter set

Table 2 Parameters used to fit both short-term and creep tests on Landes salt (the unit system is such that strain is in $\mu m/m$, stress in MPa, temperature in K and time in days)

Elastic parameters					
$E = 28,800$	$\nu = 0.32$				
Shape of the deviatoric section					
$\chi_1 = 0.7$	$\chi_2 = 0$				
Parameters of Lemaitre-type hardening mechanism					
$a = 0.29$	$k = 2.2$	$B = 0.044$	$b = 0.24$	$K = 0.13$	
Parameters related to temperature					
$A = 0$	$T_r = N/A$				
Parameters related to dilatancy					
$\nu = 0.080$	$n = 1.3$	$N = 0.012$	$m = 3.3$	$M = 1.37$	$V = 1$

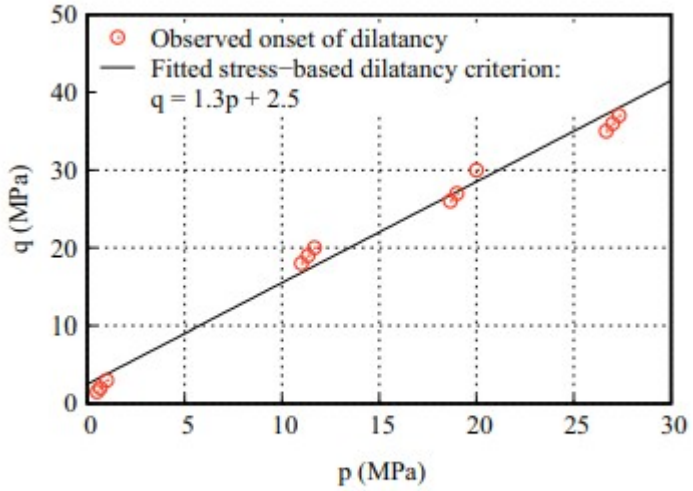

Fig. 5 Onset of dilatancy plotted in the $p - q$ plane, short-term tests on Landes salt and fitting of the stress-based criterion

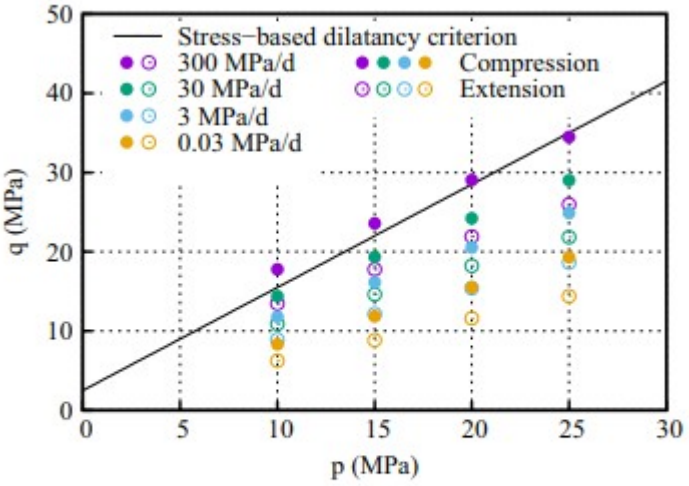

Fig. 6 Onset of dilatancy plotted in the $p - q$ plane, simulated triaxial tests

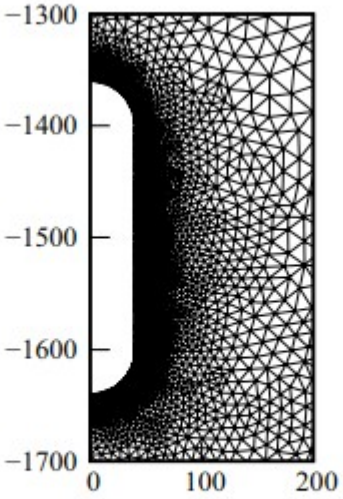

Fig. 7 Geometry and mesh of simulated cavern (close-up view around the cavern)

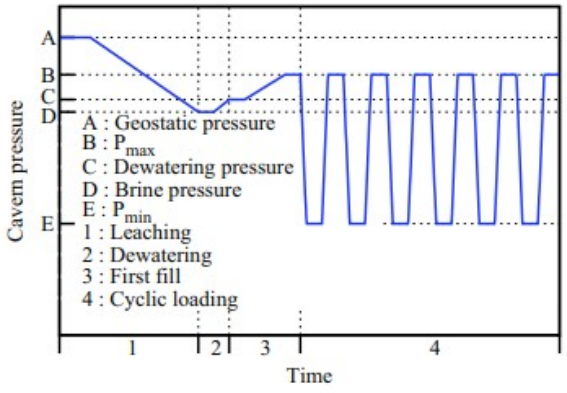

Fig. 8 Imposed cavern pressure

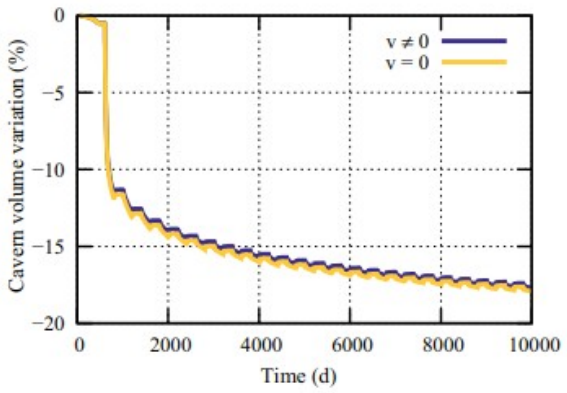

Fig. 9 Evolution of the cavern volume variation with and without the volumetric component of $\dot{\epsilon}_{vp}$ (respectively, $\nu \neq 0$ and $\nu = 0$)

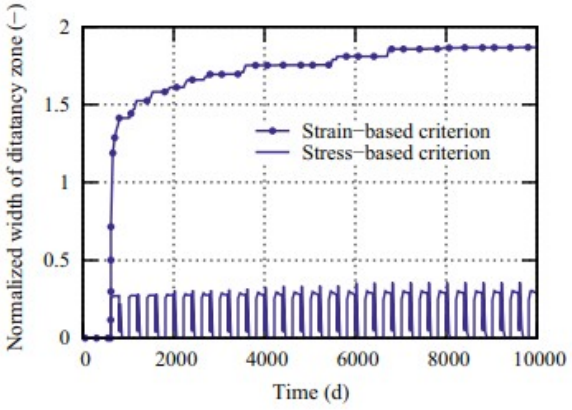

Fig. 10 Evolution of the width of the dilatancy zone normalized with respect to the radius of the cavern, according to the stress-based and the strain-based dilatancy criteria (base case scenario, $P_{min} = 0$)

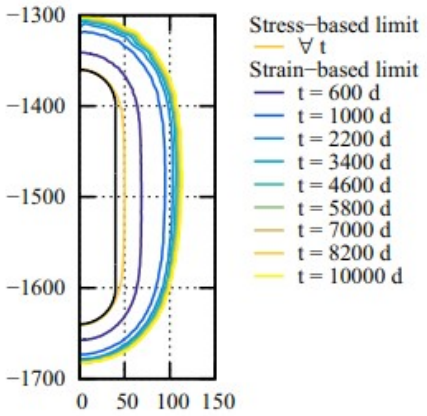

Fig. 11 Dilatancy limit around the cavern at the end of the gas withdrawal phase of different cycles, according to a stress-based and a strain-based dilatancy criteria (base case scenario, $P_{min} = 0$)

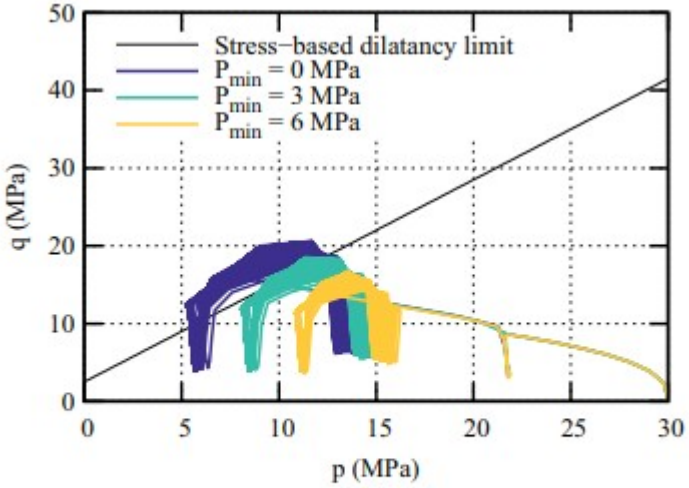

Fig. 12 Evolution of the stress state at the cavern wall for three different values of P_{min}

Fig. 13 Evolution of the width of the dilatancy zone normalized with respect to the radius of the cavern (left), and dilatancy limit around the cavern at t = 10,000 d (right), for three different values of P_{min}, according to a stress-based and a strain-based dilatancy criteria

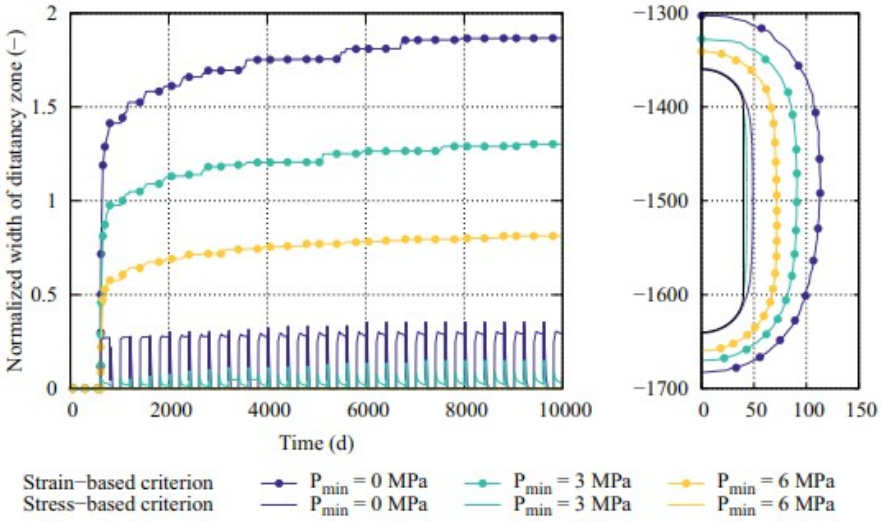

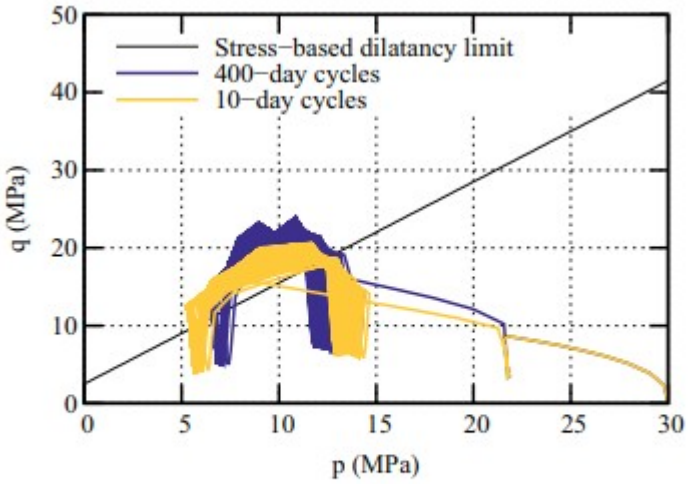

Fig. 14 Evolution of the stress state at the cavern wall for two different cycling rates

Fig. 15 Evolution of the width of the dilatancy zone normalized with respect to the radius of the cavern (left), and dilatancy limit around the cavern at $t = 10{,}000$ d (right), for two different cycling rates, according to a stress-based and a strain-based dilatancy criteria

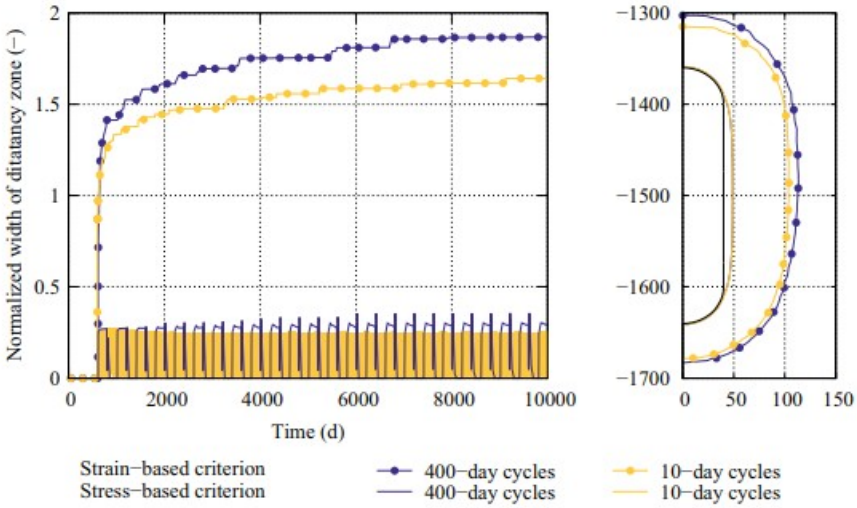

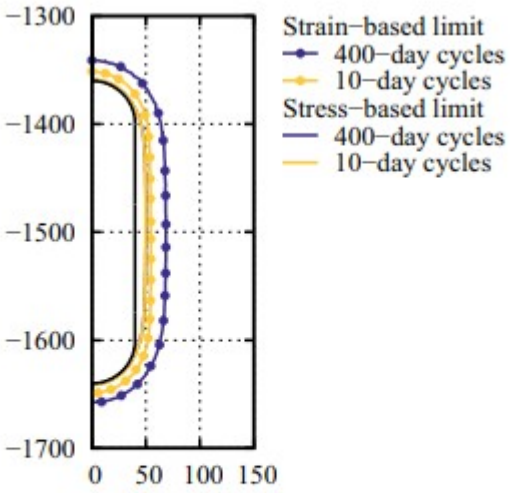

Fig. 16 Dilatancy limit around the cavern after the first gas withdrawal phase for two different cycling rates, according to a stress-based and a strain-based dilatancy criteria